RESEARCH PAPER

Hydrogen Adsorption by G-C₃N₄ and Graphene Oxide Nanosheets

Siroos Rostami, Ali Nakhaei Pour and Mohammad Izadyar

Department of Chemistry, Faculty of Science, Ferdowsi University of Mashhad, Mashhad, Iran

ARTICLE INFO

ABSTRACT

The adsorption behavior of hydrogen for synthesized graphitic carbon nitride (g-C₃N₄) and graphene oxide nanosheets was compared. The structure of the prepared g-C₃N₄ and graphene oxide samples were studied using TEM, FT-IR spectroscopy and surface area analysis. Textural results of the prepared nanosheets show that the surface area, total pore volume, and average internal diameter of g-C₃N₄ and graphene oxide samples are similar. The hydrogen adsorption isotherms at 298 K, up to 22 bar pressures were as Type III and the maximum hydrogen storage capacities at 22 bar and 296 K were 1.06 and 1.27 mmol/g for graphite oxide and g-C₃N₄ samples, respectively. The adsorption results were fitted by Freundlich model, which was related to reversible multilayer adsorption on non-uniform surface active sites with different affinities of both g-C₃N₄ and graphene oxide adsorbents. Isosteric heat of adsorption of hydrogen on the graphene oxide varies from 8.6 kJ.mol⁻¹ (at low hydrogen uptake) to 4.3 kJ.mol⁻¹. These results are the range of 10.1 to 4.8 kJ.mol⁻¹ for the prepared g-C₃N₄ sample at same hydrogen uptake. The results show that the interaction between hydrogen molecules and tri-s-triazine units in g-C₃N₄ structure are stronger than carbon atoms in graphene oxide structure.

How to cite this article

INTRODUCTION

The environment change followed by "greenhouse effect" as a result of over usage non-renewable fossil fuels away and energy challenging, encourage researchers to introduce new energy sources such as solar, wind, hydrogen and other renewable energies [1-5]. Hydrogen energy is one of the new sources, which is known as the best alternate for fossil fuels due to high internal potential, hygiene and abundance in nature, and it has been considered as a candidate for automobile industries [6]. However, hydrogen energy application has some restrictions such as volatility, safety, hard compressibility that causes any demanding in industries [7]. In the last decade, researchers took steps to overcome these problems, and they have worked for new methods for holding hydrogen in ambient temperature by adsorbents [8-12]. Currently, researchers introduced some compounds such as activated carbon [13-16], metal organic frameworks (MOFs) [17-21], graphene [22-24], carbon nanotubes [16, 25, 26], zeolites [27], metal oxide [28, 29] and other proper materials modified by doping to promote the hydrogen storage [30-32].

Hydrogen adsorption by the carbon materials such as carbon nanotubes, activated carbons, graphene and graphite were investigated in the previous works [33-35]. Now, researchers have attempted to familiarize all aspects of hydrogen storage in organic materials, especially carbon compounds because of lightweight and the affinity of hydrogen sorption by carbon atoms. It was confirmed that the replacement of some

* Corresponding Author Email: *a.nakhaei@um.ac.ir*
nakhaeipoura@yahoo.com

surface carbon atoms by B, N, S, P or Si atoms, changes the hydrogen storage ability of these compounds [36, 37]. Recently, carbon materials, including other atoms such as carbon nitride compounds have been developed. Graphitic carbon nitride (g-C$_3$N$_4$) is a family of the mixed carbon compounds with structures based on heptazine units, exhibited different properties [38, 39]. A heptazine, or tri-s-triazine includes of the three combined triazine rings, by three substituents at the corners of the triangle. The general form is 1,3,4,6,7,9,9b-heptaazaphenalene [40]. Zhu et al. reported that the graphitic carbon nitride (g-C$_3$N$_4$) could be made up by three urea, thiourea and melamine precursors [41]. It seems that the presence of other atoms in the carbon structure affects the absorption properties of these compounds.

Shadman, et al. were studied the role of silicon in the single-walled carbon nanotube structures on the hydrogen adsorption by Monte-Carlo simulations [16]. Wang et al. were studied the role of Ca, Li, Na and K atoms on the hydrogen adsorption [37, 42]

In our previous work, the structural effects of MOFs on the hydrogen adsorption were evaluated [21]. In this work, the presence of N atom's effect, as tri-s-triazine ring in carbon materials, on the hydrogen adsorption was studied. Thus, we are going to compare the hydrogen adsorption capacity of g-C$_3$N$_4$ with graphene oxide nanosheet with the same textural structures. For this purpose, we investigated all aspects of hydrogen storage, including thermodynamic variables, adsorption isotherms and industrial kinetics such as recycle life and desorption.

MATERIALS AND METHODS
Preparation of g-C$_3$N$_4$ and graphene oxide adsorbents

The g-C$_3$N$_4$ nanosheet was prepared by directly heating of urea (≥ 99.5 %, Merck) as a nitrogen-rich precursor. In detail, 100 g of urea was placed in a covered alumina container and heated to 823 K in a muffle furnace with heating rate of 5 K.min^{-1}, and then kept at this temperature for 2 h. After calcination, the yellow solid was milled, took ballet and sieved for adsorption study.

The graphene oxide nanosheet was prepared as follows. In detail, 0.5g graphite powder (purity 99%, mesh 325, Merck), and 0.5 g sodium nitrate (NaNO$_3$, Merck) were added into 23 mL sulfuric acid (H2SO4, Merck). The mixture was stirred at 278 K and then, 3.0 g of potassium permanganate (KMnO$_4$, Merck) was added to the mixture, slowly. About 40mL de-ionized water was added to the prepared suspension and was sonicated with an ultrasonic homogenizer for1 h. Finally, 100 mL de-ionized water and 3 mL hydrogen peroxide (H$_2$O$_2$, 30%, Merck) were added to the prepared suspension. The mixture filtered and washed with 250 mL HCl aqueous solution for removal of metal ions. The prepared solid was washed and dried under vacuum at 353 K for 24h, then took ballet and sieved for adsorption study.

Characterization

The structures of the prepared samples were characterized by powder X-Ray diffraction (PXRD), Fourier Transformed Infrared Spectroscopy (FT-IR), Brunauer-Emmett-Teller (BET) surface area analysis and Barrett-Joyner-Halenda (BJH) pore size and volume analysis. X-ray powder diffraction patterns were recorded on a GNR instrument using CuKα radiation (40kV, 30 mA, λ=1.54 Å) and a detector type of Detris (Fast Strip). PXRD patterns were recorded from 5 to 70° (2θ). Peak detection was performed using the JCPDS database. The distance between graphene layers was calculated using Bragg's law [43]:

$$n\lambda = 2d_{(hkl)} \sin\theta \qquad (1)$$

where ϑ is the scattering angle, λ is the X-ray wavelength, n is the order diffraction of a given reflecting plane, d is the inter planar distance of the lattices, and (h k l) are Miller indices. The mean crystallite size of the samples can be determined via Scherrer equation [44, 45]:

$$D_{hkl} = \frac{K\lambda}{\beta \cos\theta} \qquad (2)$$

where D_{hkl} is the mean size of the crystalline vertical to the (h k l) plane; β is the line broadening at half the maximum intensity (FWHM); K is a dimensionless shape factor. Nevertheless, the number of graphene layers (N) can be calculated using the Eq (3) [46, 47]:

$$N = \frac{D_{hkl}}{d_{hkl}} \qquad (3)$$

FT-IR spectra were obtained using an Avatar 370 FT-IR (Thermo Nicolet Corporation). Thin pellet for FT-IR spectra was prepared by grinding of g-G$_3$N$_4$

with potassium bromide (KBr) powder and then pressed into a disk. The results were represented in Table 1.

Brunauer-Emmett-Teller (BET) surface area and Barrett-Joyner-Halenda (BJH) pore size and volume results of the fresh prepared g-C$_3$N$_4$ sample were evaluated by N$_2$ adsorption using a Micromeritics ASAP 2010 automated system. Prior to analysis, 0.5 g of sample was degassed at 373 K for 1h, and was heated to 573 K for 2 h, and analyzed by using N$_2$ physisorption at 77 K (Table 1). The morphology of the prepared samples was observed with a transmission electron microscope (TEM, LEO 912 AB, Germany).

Adsorption measurements

Hydrogen adsorption measurements were performed using a static volumetric apparatus, which described in the previous work [21]. About 0.5 g of each sample was loaded into the sample holder and evacuated at 473 K for 120 minutes.

Then, the sample is cooled slowly to the room temperature, and the adsorption isotherm was evaluated at 298 K by using the high-purity hydrogen gas (99.999 %). The amount of adsorbed hydrogen was calculated using the ideal gas law. The compressibility factor of hydrogen in the ambient temperature and pressure was considered. To calculate the isosteric heat, the adsorption of samples was evaluated at 296, 318 and 338 K.

RESULTS AND DISCUSSION

Characterization of the prepared g-C$_3$N$_4$ and graphene oxide

PXRD patterns of the fresh prepared samples are shown in Fig. 1 (a and b). The inter planar distance of the lattice (*d*) is calculated by Eq. (1) (Bargg's law), crystallite size calculated by Eq. (2) and the number of graphene layers are calculated using Eq. (3). The calculated results are represented in Table 1.

Table 1. XRD results and textural properties of the prepared samples.

Sample	BET surface area (m^2 g^{-1})	Total pore volume (cm^3 g^{-1})	Average pore diameter (Å)	2θ(°)	d$_{hkl}$ (nm)	D$_{hkl}$ (nm)	N^a
Graphene oxide	33.2	0.17	35.4	11.7	0.78	6.38	8.4
g-C$_3$N$_4$	27.4	0.15	31.1	27.4	0.33	2.75	8.5
				13.1	0.68	----	----

a: Number of layers
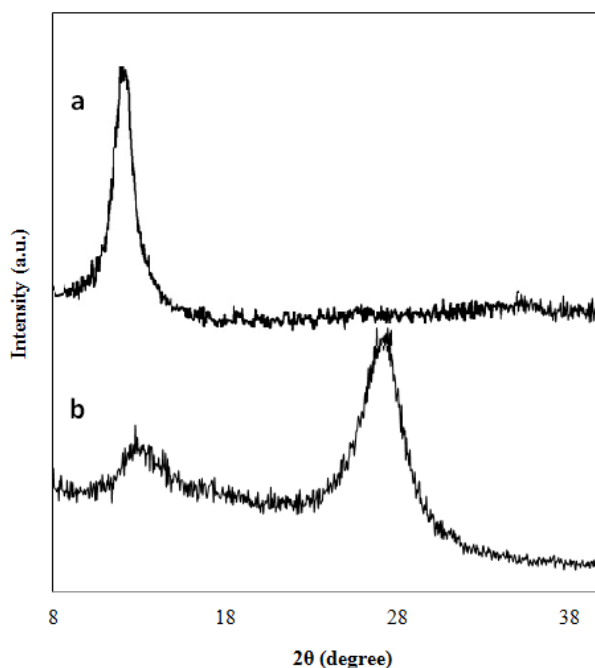
Fig. 1. XRD pattern of the prepared graphene oxide (a), and g-C$_3$N$_4$ (b)

As shown in Fig. 1.a, in the XRD pattern of the prepared graphene oxide, a strong peak is observed at 2θ = 11.7°, which is related to (002) plane with an interlayer distance (*d* spacing) of 7.8 Å and the number of layers are about 8 layers (Table 1) [47, 48]. The *d* spacing of the graphene oxide is in the range of 5 to 9 Å, which is depended on the amount of intercalated water molecules [47]. The oxidation of graphite is accompanied by an increase in *d* spacing, due to the existence of the intercalated water molecules and addition of a range of oxide groups between the layers [47, 48]. As shown in Fig. 1(*a*), there are two peaks in the XRD pattern of g-C₃N₄. The strong peak at 2θ=27.4° indexed to the (002) crystal plane [40]. This is a characteristic peak of aromatic systems with an *d* spacing of 3.3 Å (Table 1) [38, 41]. According to Table 1, the mean crystallite size and the number of layers are calculated based on (002) crystal plane position for g-C₃N₄ sample. The weak peak at 2θ=13.1° related to the (100) crystal plane. This peak was recognized to the in plane structure of tri-s-triazine units with an *d* spacing of 6.8 Å [38, 39, 41].

In FT-IR spectrum of graphene oxide prepared sample (Fig. 2, *a*), the peaks at 3400 and 3425 cm⁻¹ are related to stretching vibrations of hydroxyl groups of the water in/or between the graphene interlayer. As shown in Fig. 2 (b), the peaks at 1716 and 1048 cm⁻¹ belong to stretching vibrations of the C=O and C-O functional groups, respectively

[47, 49]. Moreover, the peak located at 1225 cm⁻¹ is related to the vibration of epoxy group and the peak at 1580 cm⁻¹ can be attributed to sp² character of the carbon atoms (C=C bonds) and the skeletal vibration of the graphene sheets, which confirm the successful oxidation of graphite [48-50].

In Fig.2, *b*, the FT-IR spectrum of the prepared g-C₃N₄ is shown. In this Fig., the broad peak between 3000- 3500 cm⁻¹ is related to the N-H stretching vibration modes, which shows the structures having the uncondensed amino functional groups. Furthermore, the region of 1200-1650 cm⁻¹ corresponds to the typical stretching modes of the CN hetero cycles [40, 41]. The peaks in 1638, 1572, 1460 and 1412 cm⁻¹ were attributed to the stretching vibration of heptazin-derived repeating units, and peaks at 1320 and 1243 cm⁻¹ indicate the out of plane bending vibration characteristic of the heptazine rings [38-41]. The band at 894 cm⁻¹ was related to deformation mode of N-H, which shows the partial condensation of amine groups [40, 41]. Finally, peak at 811 cm⁻¹ is due to the characteristic breathing mode of the tri-s-triazine unit [38, 39, 41].

Textural results of the samples are reported in the Table 1. As shown in Table 1, the BET surface area, total pore volume, and average internal diameter of g-C₃N₄ and graphene oxide samples are equal to each other. As shown in Table1, the BET specific surface area of graphene sheets is about 33.2 m² g⁻¹. However, it is lower than the
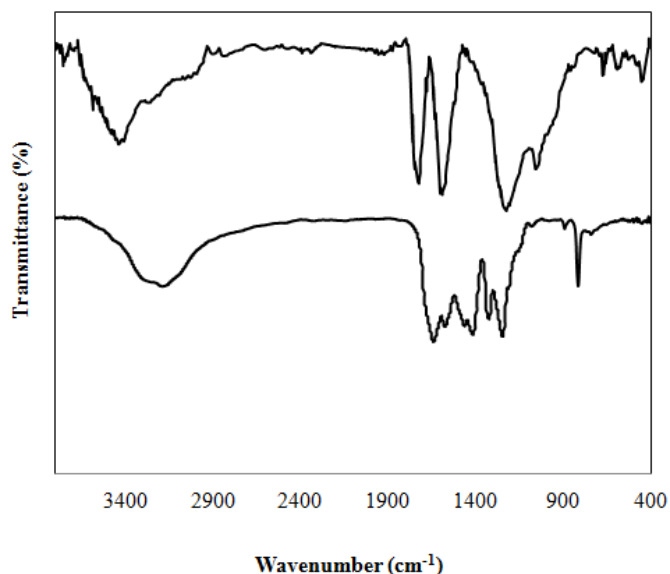
Fig. 2. FTIR spectra of the prepared graphene oxide (a), and g-C₃N₄ (b)

theoretical surface area for completely isolated graphene sheets, because of the agglomeration, overlapping and fusing the graphene sheets in the prepared sample. The specific surface area of the prepared graphene sheets is a result of the number of graphene oxide layers and high layers, confirm a lower specific surface area [51]. In addition, the BET specific surface area of the prepared g-C₃N₄ is about 27.4 $m^2 g^{-1}$. These specific surface areas are in good accordance with some reported data [40]. Given this comparable textural structure, it is expected to show like hydrogen adsorption behavior.

The N₂ adsorption-desorption isotherms of the samples are revealed in Fig. 3 (a,b). As shown in this Fig., the prepared g-C₃N₄ and graphene oxide samples obviously show type IV of IUPAC classification isotherms with H₃ hysteresis loops. This form indicates the presence of mesopores and arrangement of slit-shaped pores from aggregates off the lake-like particles [52].

The pore size distribution (PSD) of the prepared g-C₃N₄ and graphene oxide samples, obtained from the adsorption division of the BJH isotherm, is revealed in Fig. 4 (a,b). The PSD of the samples shows major peaks in the micropores, mesopores and macropores regions. The main pore size in the BJH curve of the graphene oxide belongs to
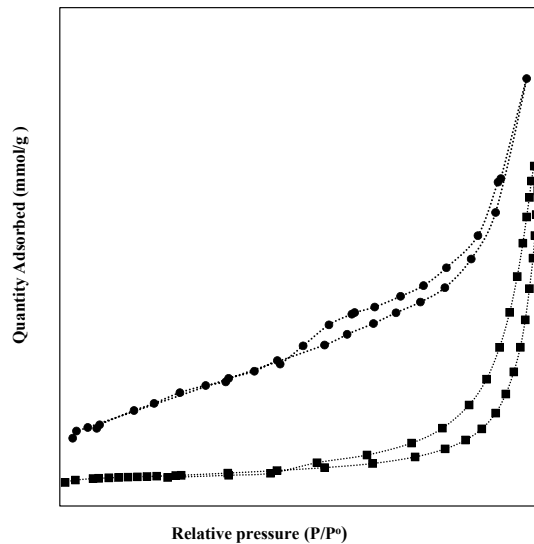
Fig. 3. Nitrogen adsorption–desorption isotherms of the graphene oxide (●) and g-C₃N₄ (■) samples obtained at 77 K
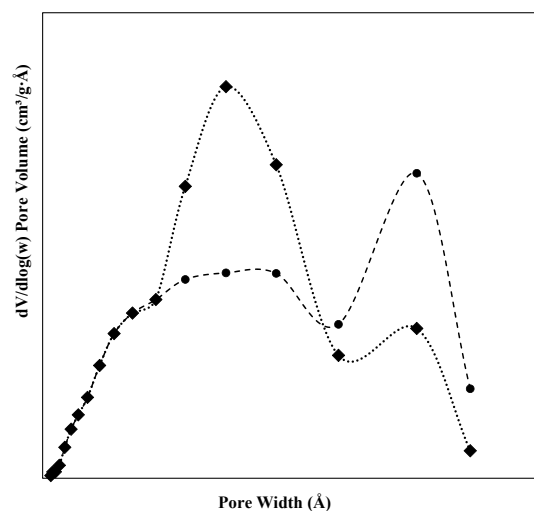
Fig. 4. The pore size distribution (PSD) of the graphene oxide (■) and g-C₃N₄ (●) samples

mesoporous (2–50 nm), which are a key grouping of the nanoporous materials [52]. A broad peak centered at about 50 nm can be shown in the BJH curve of the g-C$_3$N$_4$. The presence of macropores and mesopores is originated from the H$_2$S and H$_2$O released during the heating of urea.

The morphologies of the prepared graphene oxide and g-C$_3$N$_4$ nanosheets were evaluated by TEM observation. Fig. 5 (a, b) shows the TEM images of the graphene oxide and g-C$_3$N$_4$ samples. As shown in Fig. 5, the prepared graphene oxide and g-C$_3$N$_4$ sheets are not completely flat and prove intrinsic microscopic irregularity. Moreover, the semitransparent and lined sheets exhibit few layer planar sheets in both samples.

Hydrogen adsorption

The prepared graphene oxide and g-C$_3$N$_4$ samples were degassed at 473 K for 120 minutes before hydrogen adsorption. The hydrogen adsorption isotherms obtained using the volumetric analysis at 298 K and up to 22 bar pressure, are shown in Fig. 6. As shown in Fig. 6, these hydrogen adsorption isotherms are obviously of type III of Brunauer's classification, which are consistent with different pore regions in the prepared samples [52]. There is no flattish part in the curve, which prove that monolayer formation is absent and this isotherm, which explains the formation of multilayer adsorption. Therefore, this type of isotherm shows large deviation from the Langmuir
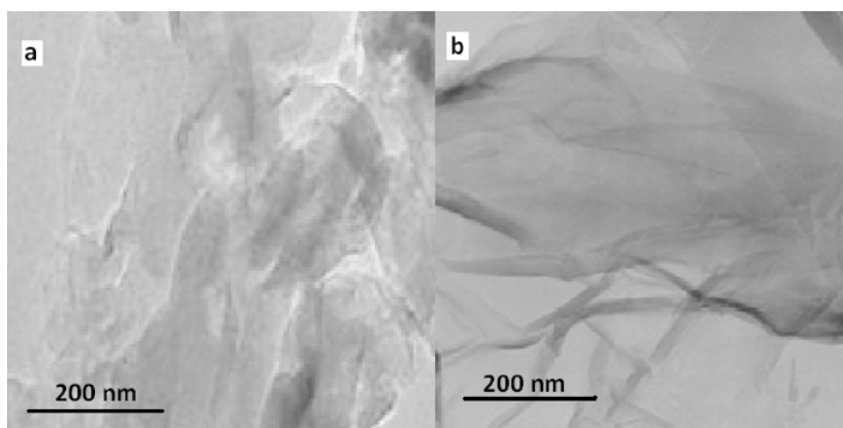
Fig. 5. TEM images of the g-C$_3$N$_4$ (a) and graphene oxide (b)
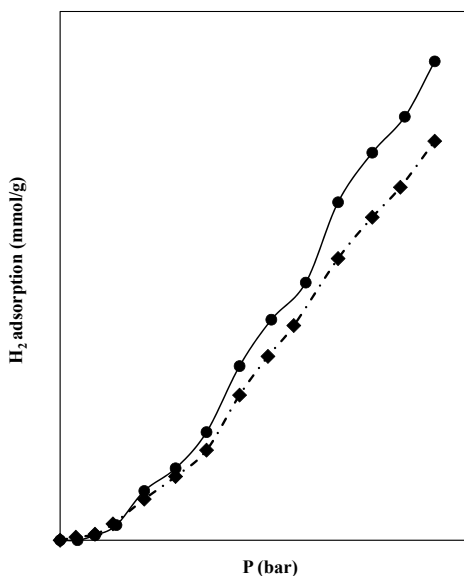
Fig. 6. Hydrogen adsorption isotherms of the graphene oxide (■) and g-C$_3$N$_4$ (●) samples at 298 K and pressures up to 22 bar

model [52, 53]. The isotherms (in Fig. 6) show that the upper limit hydrogen storage capacities are 1.06 and 1.27 mmol/g for graphene oxide and g-C₃N₄ samples at 22 bar and 296 K, respectively. These results showed that the adsorption ability of the g-C₃N₄ sample was higher than graphene oxide adsorbent. These results for graphene oxide at 296 K are comparable with the earlier reports [54-56]. In addition, these results showed that the presence of N atoms in the g-C₃N₄ structure (in the tri-s-triazine units) increases the hydrogen storage more than similar carbon materials [11, 57].

Fig. 7 shows the temperature effect on the hydrogen adsorption on the graphene oxide and prepared g-C₃N₄ sample. As shown in this figure, the amount of hydrogen adsorptions on both samples decrease rapidly from 296 to 338 K. The experiments were carried out in three temperatures of 296, 318 and 338 K to determine the effect of temperature on the hydrogen adsorption.

To describe the adsorption processes of hydrogen on the g-C₃N₄ and graphene oxide adsorbents, the Freundlich and the Temkin isotherm models were used. The Freundlich model is regularly used for heterogeneous adsorption and is known by Eq. (4) [58]:

$$Q_m = k_f P^{\frac{1}{n}} \tag{4}$$

Where, k_f is the Freundlich adsorption coefficient for adsorption capacity, n is the adsorption constant that characterizes the adsorption strength and energy division of the adsorption sites, Q_m is the amount of adsorption and P is the pressure of adsorption. The Temkin isotherm model describes the adsorption behavior on the heterogeneous surfaces and is given by Eq. (5) [58]:

$$Q_m = \frac{RT}{b} \ln(CP) \tag{5}$$
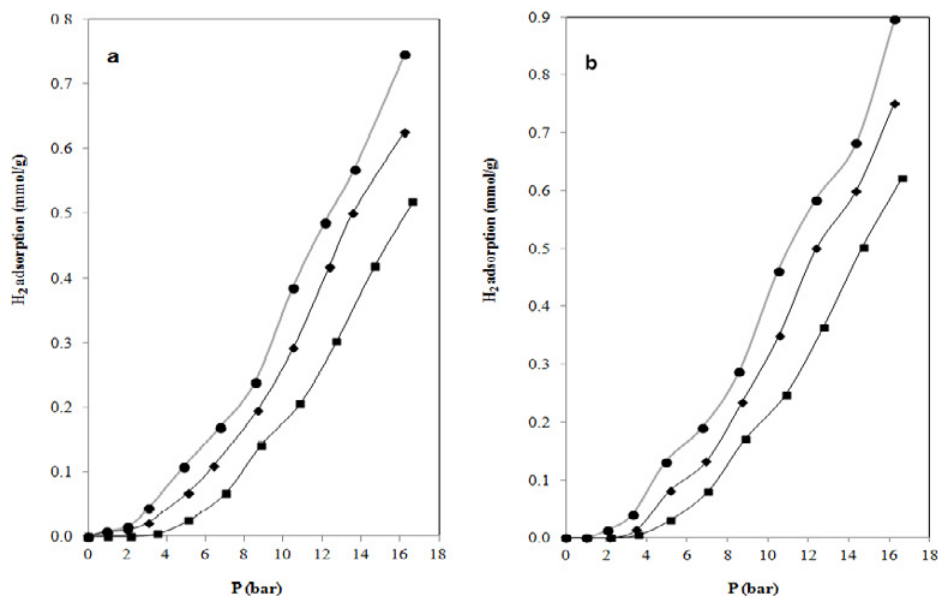
Fig. 7. Hydrogen adsorption isotherms of the graphene oxide (a) and g-C₃N₄ (b) prepared samples at 298 K (●), 318 K (♦) 338 K (■) and pressures up to 16.3 bar

Table 2. Adsorption parameters of the prepared samples 296, 318 and 338 K.

Sample	Temperature (K)	Freundlich isotherm			Temkin isotherm		
		k_f	n	R^2	b	C	R^2
g-C₃N₄	296	3.9×10^{-3}	0.502	0.987	4.6×10^3	0.292	0.750
	318	1.1×10^{-3}	0.411	0.961	5.4×10^3	0.252	0.728
	338	1.8×10^{-4}	0.333	0.972	6.4×10^3	0.203	0.665
Graphene oxide	296	7.1×10^{-3}	0.600	0.989	4.5×10^3	0.240	0.748
	318	4.1×10^{-3}	0.560	0.977	5.3×10^3	0.207	0.720
	338	1.5×10^{-4}	0.333	0.972	6.5×10^3	0.169	0.665

where, *b* is the Temkin constant that is associated with the heat of adsorption; *C* is the adsorption constant; *R* is the gas constant (8.314 J.mol^{-1} K^{-1}), *T* are temperature (K) and *P* is the pressure of adsorption. The basis of the Temkin isotherm is based on the linear decrease in the absorption energy by increasing the surface coverage due to adsorbent-adsorbate interactions. Moreover, the Freundlich isotherm model is derived from the assumption that the adsorption energy exponentially decreases with the surface occupation because of non-uniform distribution affinities over the heterogeneous surface. The fitting results of the experimental data and calculated parameters of Temkin and Freundlich isotherms are given in Table 2. The R-squared value is used for comparison of the models in Table 2. As shown in Table 2, data were improved fitted to Freundlich model in comparison to the Temkin model due to a higher R-squared value for both g-C$_3$N$_4$ and graphene oxide adsorbents. This condition indicates that the adsorption mechanism is correlated to reversible multilayer adsorption with non-identical distribution of the adsorption affinities over the heterogeneous surface of both g-C$_3$N$_4$ and graphene oxide adsorbents. As shown in Table 2, the Freundlich adsorption constant (n) of the g-C$_3$N$_4$ adsorbent is lower than that of graphene oxide adsorbent, while the Temkin constant (b) of the g-C$_3$N$_4$ adsorbent is higher than that of graphene oxide adsorbent. These results show that the strength of the adsorption sites of g-C$_3$N$_4$ is higher than that of graphene oxide. However, at a higher temperatures, these adsorbents exhibit the same absorption behavior.

Carbon materials store hydrogen in different mechanisms. In mechanism I, hydrogen is adsorbed at the surface of the material which demonstrates the interaction between hydrogen and carbon surfaces [59]. In mechanism II, the hydrogen molecules permeate into the space between carbon layers. The results show that the hydrogen absorbed through the mechanisms of I and II on the surfaces of both g-C$_3$N$_4$ and Graphene oxide.

Isosteric heat of adsorption

Isosteric heat of hydrogen adsorption on the adsorbents represents the connections between the hydrogen molecules and the adsorbents. The previous works show that the isosteric heat of hydrogen molecules on the graphene oxide nanosheets is in the range of 4 to 6 kJ.mol^{-1} [12, 60-62].

The isosteric heat of adsorption (Q_a) of hydrogen molecules is considered from the temperature reliance of hydrogen adsorption isotherms, by means of the Clausius– Clapeyron equation (Eq.6).

$$[\frac{d \ln p}{d(\frac{1}{T})}]_\theta = \frac{Q_a}{R} \tag{6}$$

where, *P* is the saturation pressure of adsorption; *R* is the specific gas constant, *T* is the absolute temperature of adsorption; Q_a is the isosteric heat of adsorption and ϑ is the surface coverage. It should be noted that the adsorption enthalpy must be calculated at a constant surface
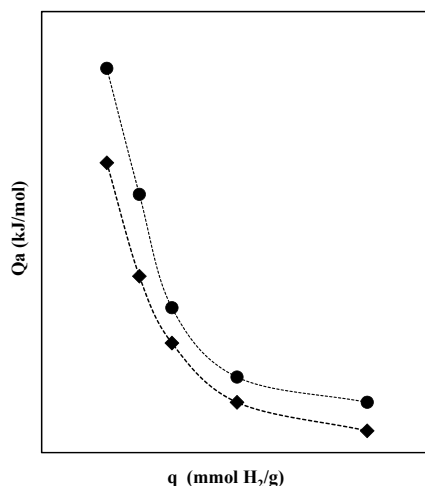
Fig. 8. Isosteric heat of adsorption versus adsorption capacity, graphene oxide (▪) and g-C$_3$N$_4$ (●)
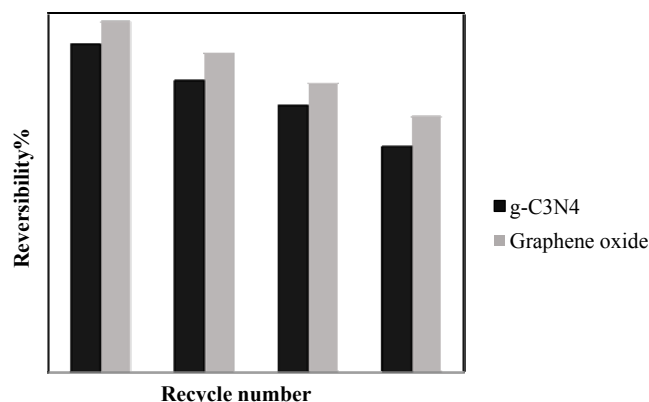
Fig. 9. Reversibility% for g-C$_3$N$_4$ and graphene oxide samples

coverage. The variation of the isosteric heat of adsorption (Q_a) with the amount of hydrogen adsorption capacity (mmol/g) is shown in Fig. 8. Generally, isosteric heat of adsorption decreases with surface coverage increasing.

As revealed in Fig. 8, isosteric heat of hydrogen adsorption on the graphene oxide is in the range of 8.6 kJ.mol^{-1} (at low hydrogen uptake) to 4.3 kJ.mol^{-1} (at fair uptake). In addition, the related results for g-C$_3$N$_4$ are in the range of 10.1 to 4.8 kJ.mol^{-1} (at same hydrogen uptake). These results are comparable with the results of the hydrogen physisorption on the carbon adsorbents [24, 54, 55, 63]. These results show that the method used to evaluate the adsorption of hydrogen at C$_3$N$_4$ and graphene oxide surfaces is of prime importance. Based on these results, the interaction of hydrogen molecules and tri-s-triazine units in the g-C$_3$N$_4$ structure are stronger than carbon atoms in graphene oxide structure [57, 64].

Desorption process and recycle life

The reversibility and recycling process are two important kinetically factors in evaluating the performance of an absorbent. Good hydrogen adsorbent in industrial application, not only must adsorb high amount of hydrogen molecules in the adsorption step, but also, it must almost release all of hydrogen molecules in the desorption step. Fig. 9 shows the reversibility (%) of the g-C$_3$N$_4$ and graphene oxide samples. As shown in this figure, the reversibility of g-C$_3$N$_4$ and graphene oxide samples at the first cycle were about 30 and 28%. Moreover, the reversibility of the studied samples, after 4 cycles, reduces to 22% and 19% for graphene oxide and g-C$_3$N$_4$, respectively. According to United States Department of Energy (USDOE)

the recycle life of the adsorbent used in the on-board light vehicle must be 1500 cycles with at least 60% hydrogen desorption [65]. On the base of the obtained data, it can be concluded that the stability of pure g-C$_3$N$_4$ for hydrogen sorption is less than graphene oxide.

CONCLUSIONS

In this study, the effects of N atoms of the tri-s-triazine rings in carbon materials on the hydrogen adsorption were studied. For this purpose, the hydrogen adsorption behaviors of the g-C$_3$N$_4$ with graphene oxide nanosheets were compared. The results show that the structural and textural properties of the s g-C$_3$N$_4$ with graphene oxide nanosheets, XRD results, surface area, total pore volume, and typical internal distance of g-C$_3$N$_4$ and graphene oxide samples are nearly equal. The BET specific surface area of the prepared g-C$_3$N$_4$ and graphene oxide samples are about 27.4 and 33.2 m^2 g^{-1}, respectively. The nitrogen adsorption-desorption isotherms show type IV of the IUPAC classification isotherms with H$_3$ hysteresis loops. This type indicates the existence of mesopores and arrangement of opening shaped pores from aggregates of the lake-like particles. The TEM images of the graphene oxide and g-C$_3$N$_4$ samples show that these samples are not completely flat and prove basic microscopic roughness. In addition, semitransparent and creased sheets exhibit few layer planar sheets in both samples.

The hydrogen adsorption isotherms for both samples are clearly of Type III of Brunauer's classification, which are consistent with different pore regions in the prepared samples. There is no flat part in the curve, which proves that the monolayer configuration is not present, and this

isotherm explains the formation of multilayer adsorption. The isotherms show that the highest hydrogen capacities are 1.06 and 1.27 mmol/g for graphene oxide and g-C$_3$N$_4$ samples at 22 bar and 296 K, respectively. The hydrogen adsorption data were superior fitted by Freundlich model, representing that the adsorption mechanism is related to reversible multilayer adsorption with non-identical distribution of the adsorption affinities over the heterogeneous surface of both g-C$_3$N$_4$ and graphene oxide adsorbents. The Freundlich adsorption constant (n) of the g-C$_3$N$_4$ adsorbent is lower than that of graphene oxide adsorbent, while the Temkin constant (b) of the g-C$_3$N$_4$ adsorbent is more than that of graphene oxide adsorbent. These results show that the adsorption strengths of the adsorption sites of the g-C$_3$N$_4$ are more than that of graphene oxide. However, at higher temperatures, these adsorbents exhibit similar absorption behavior. Isosteric heat of adsorption of hydrogen on the graphene oxide and g-C$_3$N$_4$ is in the range of 8.6 kJ.mol^{-1} - 4.3 kJ.mol^{-1} and 10.1 - 4.8 kJ.mol^{-1}, respectively. These consequences show that the communication between of the H$_2$ molecules and tri-s-triazine units of the g-C$_3$N$_4$ structure are stronger than carbon atoms in graphene oxide structure.

ACKNOWLEDGEMENT

CONFLICT OF INTEREST

The authors declare that there are no conflicts of interest regarding the publication of this manuscript.

REFERENCES

1. Kardooni R, Yusoff SB, Kari FB, Moeenizadeh L. Public opinion on renewable energy technologies and climate change in Peninsular Malaysia. Renewable Energy. 2018;116:659-668.
2. Howard BS, Hamilton NE, Diesendorf M, Wiedmann T. Modeling the carbon budget of the Australian electricity sector's transition to renewable energy. Renewable Energy. 2018;125:712-728.
3. Das V, Padmanaban S, Venkitusamy K, Selvamuthukumaran R, Blaabjerg F, Siano P. Recent advances and challenges of fuel cell based power system architectures and control–A review. Renewable and Sustainable Energy Reviews. 2017;73:10-18.
4. Nakhaei Pour A, Housaindokht MR, Garmroodi Asil A. Production of Higher Hydrocarbons from CO2 over Nanosized Iron Catalysts. Chemical Engineering & Technology. 2018;41:479-488.
5. Nakhaei Pour A, Housaindokht MR, Monhemi H. A new LHHW kinetic model for CO$_2$ hydrogenation over an iron catalyst. Progress in Reaction Kinetics and Mechanism. 2016;41:159-169.
6. Chilev C, Lamari FD. Hydrogen storage at low temperature and high pressure for application in automobile manufacturing. International Journal of Hydrogen Energy. 2016;41:1744-1758.
7. Yakovenko IS, Ivanov MF, Kiverin AD, Melnikova KS. Large-scale flame structures in ultra-lean hydrogen-air mixtures. International Journal of Hydrogen Energy. 2018;43:1894-1901.
8. Nakhaei Pour A, Mousavi M. Combined reforming of methane by carbon dioxide and water: Particle size effect of Ni–Mg nanoparticles. Int J Hydrogen Energy. 2015;40:12985-12992.
9. Nakhaei Pour A, Keyvanloo Z, Izadyar M, Modaresi SM. Dissociative hydrogen adsorption on the cubic cobalt surfaces: A DFT study. International Journal of Hydrogen Energy. 2015;40:7064-7071.
10. Nakhaei Pour A, Karimi J, Taghipoor S, Gholizadeh M, Hashemian M. Fischer–Tropsch synthesis over CNT-supported cobalt catalyst: effect of magnetic field. Journal of the Iranian Chemical Society. 2017;14:1477-1488.
11. Zhou Y, Chu W, Jing F, Zheng J, Sun W, Xue Y. Enhanced hydrogen storage on Li-doped defective graphene with B substitution: A DFT study. Appl Surf Sci. 2017;410:166-176.
12. Zhou W, Wu H, Hartman MR, Yildirim T. Hydrogen and methane adsorption in metal– organic frameworks: a high-pressure volumetric study. The Journal of Physical Chemistry C. 2007;111:16131-16137.
13. Youssef AM, El-Nabarawy T, Samra SE. Sorption properties of chemically-activated carbons: 1. Sorption of cadmium(II) ions. Colloids and Surfaces A: Physicochemical and Engineering Aspects. 2004;235:153-163.
14. Imran Din M, Ashraf, S. and Initsar, A. . a review of ways of making activated carbon from readily available materials. Science progress , . 2017;100:299-312.
15. Xia K, Hu J, Jiang J. Enhanced room-temperature hydrogen storage in super-activated carbons: The role of porosity development by activation. Applied Surface Science. 2014;315:261-267.
16. Shadman M, Yeganegi S, Galugahi MR. Hydrogen physisorption and selectivity in single-walled silicon carbon nanotubes: a grand canonical Monte-Carlo study. Journal of the Iranian Chemical Society. 2016;13:207-220.
17. Abid HR, Rada ZH, Shang J, Wang S. Synthesis, characterization, and CO$_2$ adsorption of three metal-organic frameworks (MOFs): MIL-53, MIL-96, and amino-MIL-53. Polyhedron. 2016;120:103-111.
18. Saha D, Deng S. Synthesis, characterization and hydrogen adsorption in mixed crystals of MOF-5 and MOF-177. international journal of hydrogen energy. 2009;34:2670-2678.
19. Li J, Cheng S, Zhao Q, Long P, Dong J. Synthesis and hydrogen-storage behavior of metal–organic framework MOF-5. International Journal of Hydrogen Energy. 2009;34:1377-1382.
20. Bordiga S, Vitillo JG, Ricchiardi G, Regli L, Cocina D, Zecchina A, Arstad B, Bjørgen M, Hafizovic J, Lillerud KP. Interaction of Hydrogen with MOF-5. The Journal of Physical Chemistry

B. 2005;109:18237-18242.

21. Rostami S, Nakhaei Pour A, Salimi A, Abolghasempour A. Hydrogen adsorption in metal- organic frameworks (MOFs): Effects of adsorbent architecture. International Journal of Hydrogen Energy. 2018;43:7072-7080.

22. Kostoglou N, Tzitzios V, Kontos AG, Giannakopoulos K, Tampaxis C, Papavasiliou A, Charalambopoulou G, Steriotis T, Li Y, Liao K, Polychronopoulou K, et al. Synthesis of nanoporous graphene oxide adsorbents by freeze-drying or microwave radiation: Characterization and hydrogen storage properties. Int J Hydrogen Energy. 2015;40:6844-6852.

23. Guo J-H, Liu D-D, Li X-D, Liu H-Y, Chen G. Pt4, Pd4, Ni4, and Ti4 catalyzed hydrogen spillover on penta-graphene for hydrogen storage: The first-principles and kinetic Monte Carlo study. Int J Hydrogen Energy. 2017.

24. Rudolf KSnADGnAP. Hydrogen Storage in Graphene-Based Materials: Efforts Towards Enhanced Hydrogen Absorption. ECS Journal of Solid State Science and Technology. 2013.

25. Silambarasan D, Surya VJ, Vasu V, Iyakutti K. Investigation of single-walled carbon nanotubes-titanium metal composite as a possible hydrogen storage medium. Int J Hydrogen Energy. 2013;38:14654-14660.

26. Khoshnevisan B, Yazdani Kachoei M, Mohammadi M. Diameter and chirality effects of narrow SWCNTs on molecular hydrogenation. Int J Hydrogen Energy. 2013;38:4618-4621.

27. Fellah MF. A DFT study of hydrogen adsorption on Be, Mg and Ca frameworks in erionite zeolite. Applied Surface Science. 2017;394:9-15.

28. Rather Su. Hydrogen uptake of cobalt and copper oxide-multiwalled carbon nanotube composites. Int J Hydrogen Energy. 2017;42:11553-11559.

29. Enriquez JIG, Villagracia ARC. Hydrogen adsorption on pristine, defected, and 3d-block transition metal-doped penta-graphene. Int J Hydrogen Energy. 2016;41:12157-12166.

30. Salehabadi A, Salavati-Niasari M, Ghiyasiyan-Arani M. Self-assembly of hydrogen storage materials based multi-walled carbon nanotubes (MWCNTs) and Dy₃Fe₅O₁₂ (DFO) nanoparticles. Journal of Alloys and Compounds. 2018;745:789-797.

31. Ghiyasiyan-Arani M, Salavati-Niasari M. Effect of Li₂CoMn₃O₈ nanostructures synthesized by a combustion method on montmorillonite K10 as a potential hydrogen storage material. The Journal of Physical Chemistry C. 2018;122:16498-16509.

32. Mazloom F, Ghiyasiyan-Arani M, Monsef R, Salavati-Niasari M. Photocatalytic degradation of diverse organic dyes by sol–gel synthesized Cd₂V₂O₇ nanostructures. Journal of Materials Science: Materials in Electronics.1-8.

33. Zubizarreta L, Arenillas A, Pis JJ. Carbon materials for H₂ storage. Int J Hydrogen Energy. 2009;34:4575-4581.

34. Yuan J, Zhu Y, Li Y, Zhang L, Li L. Effect of multi-wall carbon nanotubes supported palladium addition on hydrogen storage properties of magnesium hydride. Int J Hydrogen Energy. 2014;39:10184-10194.

35. Xiao Y, Dong H, Long C, Zheng M, Lei B, Zhang H, Liu Y. Melaleuca bark based porous carbons for hydrogen storage. Int J Hydrogen Energy. 2014;39:11661-11667.

36. Lotfi R, Saboohi Y. Effect of metal doping, boron substitution and functional groups on hydrogen adsorption of MOF-5: A DFT-D study. CompTheo Chem. 2014;1044:36-43.

37. Wang J, Du Y, Sun L. Ca-decorated novel boron sheet: A potential hydrogen storage medium. Int J Hydrogen Energy. 2016;41:5276-5283.

38. Yuan X, Zhou C, Jin Y, Jing Q, Yang Y, Shen X, Tang Q, Mu Y, Du A-K. Facile synthesis of 3D porous thermally exfoliated g-C₃N₄ nanosheet with enhanced photocatalytic degradation of organic dye. Journal of Colloid and Interface Science. 2016;468:211-219.

39. Yan SC, Li ZS, Zou ZG. Photodegradation Performance of g-C₃N₄ Fabricated by Directly Heating Melamine. Langmuir. 2009;25:10397-10401.

40. Wang A, Wang C, Fu L, Wong-Ng W, Lan Y. Recent Advances of Graphitic Carbon Nitride-Based Structures and Applications in Catalyst, Sensing, Imaging, and LEDs. Nano-Micro Letters. 2017;9:47.

41. Zhu B, Xia P, Ho W, Yu J. Isoelectric point and adsorption activity of porous g-C3N4. Appl Surf Sci. 2015;344:188-195.

42. Wang L, Chen X, Du H, Yuan Y, Qu H, Zou M. First-principles investigation on hydrogen storage performance of Li, Na and K decorated borophene. Applied Surface Science. 2018;427:1030-1037.

43. Crews C, Kenny PS, O'Flynn D, Speller RD. Multivariate calibration of energy-dispersive X-ray diffraction data for predicting the composition of pharmaceutical tablets in packaging. Journal of Pharmaceutical and Biomedical Analysis. 2018;151:186-193.

44. Nakhaei Pour A, Gholizadeh M, Housaindokht M, Moosavi F, Monhemi H. A new method for preparing mono-dispersed nanoparticles using magnetized water. Appl Phys A. 2017;123:269.

45. Nakhaei Pour A, Housaindokht MR. A new kinetic model for direct CO2 hydrogenation to higher hydrocarbons on a precipitated iron catalyst: Effect of catalyst particle size. Journal of Energy Chemistry. 2017;26:359-367.

46. Alasvand Zarasvand K, Golestanian H. Investigating the effects of number and distribution of GNP layers on graphene reinforced polymer properties: Physical, numerical and micromechanical methods. Composites Science and Technology. 2017;139:117-126.

47. Jabari Seresht R, Jahanshahi M, Rashidi A, Ghoreyshi AA. Synthesize and characterization of graphene nanosheets with high surface area and nano-porous structure. Applied Surface Science. 2013;276:672-681.

48. Esmaeili A, Entezari MH. Facile and fast synthesis of graphene oxide nanosheets via bath ultrasonic irradiation. Journal of Colloid and Interface Science. 2014;432:19-25.

49. Gu D, Fein JB. Adsorption of metals onto graphene oxide: Surface complexation modeling and linear free energy relationships. Colloid Surface A. 2015;481:319-327.

50. Das TK, Banerjee S, Pandey M, Vishwanadh B, Kshirsagar RJ, Sudarsan V. Effect of surface functional groups on hydrogen adsorption properties of Pd dispersed reduced graphene oxide. Int J Hydrogen Energy. 2017;42:8032-8041.

51. Chabot V, Higgins D, Yu A, Xiao X, Chen Z, Zhang J. A review of graphene and graphene oxide sponge: material synthesis and applications to energy and the environment. Energy & Environmental Science. 2014;7:1564-1596.

52. Sing KSW. Adsorption methods for the characterization of porous materials. Advances in Colloid and Interface Science. 1998;76-77:3-11.

53. Aranovich G, Donohue M. Analysis of Adsorption Isotherms: Lattice Theory Predictions, Classification of Isotherms for

Gas–Solid Equilibria, and Similarities in Gas and Liquid Adsorption Behavior. Journal of Colloid and Interface Science. 1998;200:273-290.

54. Srinivas G, Zhu Y, Piner R, Skipper N, Ellerby M, Ruoff R. Synthesis of graphene-like nanosheets and their hydrogen adsorption capacity. Carbon. 2010;48:630-635.

55. Ma L-P, Wu Z-S, Li J, Wu E-D, Ren W-C, Cheng H-M. Hydrogen adsorption behavior of graphene above critical temperature. International Journal of Hydrogen Energy. 2009;34:2329-2332.

56. Xu WC, Takahashi K, Matsuo Y, Hattori Y, Kumagai M, Ishiyama S, Kaneko K, Iijima S. Investigation of hydrogen storage capacity of various carbon materials. International Journal of Hydrogen Energy. 2007;32:2504-2512.

57. Zhang W, Zhang Z, Zhang F, Yang W. Ti-decorated graphitic-C$_3$N$_4$ monolayer: A promising material for hydrogen storage. Appl Surf Sci. 2016;386:247-254.

58. Gao Y, Li Y, Zhang L, Huang H, Hu J, Shah SM, Su X. Adsorption and removal of tetracycline antibiotics from aqueous solution by graphene oxide. Journal of Colloid and Interface Science. 2012;368:540-546.

59. Li Y, Zhao D, Wang Y, Xue R, Shen Z, Li X. The mechanism of hydrogen storage in carbon materials. Int J Hydrogen Energy. 2007;32:2513-2517.

60. Panella B, Hirscher M, Pütter H, Müller U. Hydrogen Adsorption in Metal Organic Frameworks: Cu-MOFs and Zn-MOFs Compared. Advanced Functional Materials. 2006;16:520-524.

61. Sillar K, Hofmann A, Sauer J. Ab initio study of hydrogen adsorption in MOF-5. Journal of the American Chemical Society. 2009;131:4143-50.

62. Rowsell JL, Spencer EC, Eckert J, Howard JA, Yaghi OM. Gas adsorption sites in a large-pore metal-organic framework. Science. 2005;309:1350-1354.

63. Panella B, Hirscher M, Roth S. Hydrogen adsorption in different carbon nanostructures. Carbon. 2005;43:2209-2214.

64. Gao J, Ngene P, Herrich M, Xia W, Gutfleisch O, Muhler M, de Jong KP, de Jongh PE. Interface effects in NaAlH4–carbon nanocomposites for hydrogen storage. Int J Hydrogen Energy. 2014;39:10175-10183.

65. Hydrogen Energy. Mechanical Engineers' Handbook.